materials

MDPI

Article

Growth, Structure and Optical Characterization of $Rb_3Ti_3P_5O_{20}$ Single Crystal

Jianfu Zhao, Pengfei Zhu, Zhenyan Wang, Li Ai, Xiulan Duan * and Fapeng Yu

State Key Laboratory of Crystal Materials, Institute of Crystal Materials, Shandong University, Jinan 250100, China; 202012909@mail.sdu.edu.cn (J.Z.); joseph.zhu.nt@gmail.com (P.Z.); wangzhenyan@mail.sdu.edu.cn (Z.W.); 201912593@mail.sdu.edu.cn (L.A.); fapengyu@sdu.edu.cn (F.Y.)
* Correspondence: xlduan@sdu.edu.cn

Abstract: Phosphate crystals attract much attention on account of their rich crystal structures and excellent physical and chemical properties. Herein, $Rb_3Ti_3P_5O_{20}$ single crystals were grown by the high temperature solution method using Rb_2CO_3 and $NH_4H_2PO_4$ as the fluxes. This crystal, with non-centrosymmetric $Pca2_1$ space group, presents a three-dimensional framework structure composed of [TiO_6] octahedron, [PO_4] tetrahedra, and [P_2O_7] dimers. The electronic structure was measured via X-ray photoelectron spectroscopy. The measurements found that $Rb_3Ti_3P_5O_{20}$ has stronger Ti–O ionic bonding properties and weaker P–O covalent bonding properties compared to $RbTiOPO_4$. Optical measurements indicated that $Rb_3Ti_3P_5O_{20}$ has a 3.54 eV band gap and a wide transmission range (0.33–4.5 μm). Theoretical calculations showed that $Rb_3Ti_3P_5O_{20}$ crystals have a moderate birefringence of 0.079 at 1064 nm. In addition, the relationship of the structure–property was studied using first-principles method. The results demonstrated that TiO_6 octahedron played a significant role for the optical properties.

Keywords: phosphate; single crystal growth; electronic structure; optical properties

Citation: Zhao, J.; Zhu, P.; Wang, Z.; Ai, L.; Duan, X.; Yu, F. Growth, Structure and Optical Characterization of $Rb_3Ti_3P_5O_{20}$ Single Crystal. *Materials* **2022**, *15*, 5346. https://doi.org/10.3390/ma15155346

Academic Editor: Fortunato Neri

Received: 11 July 2022
Accepted: 29 July 2022
Published: 3 August 2022

1. Introduction

Inorganic phosphate materials have received considerable attention due to their rich structures and excellent physicochemical properties, as well as possessing broad applications in the fields of nonlinear optics, ferroelectricity, luminescence, energy technologies, and catalysts [1–5]. For instance, $KTiOPO_4$ (KTP) and KH_2PO_4 (KDP) crystals have been used for solid-state lasers as important nonlinear optical materials, and olivine-type $LiFePO_4$ is an outstanding cathode material for rechargeable Lithium batteries with high capacity [6–8]. In the structure of phosphate materials, one P atom is generally coordinated with four O atoms to shape into the [PO_4] tetrahedra. These [PO_4] tetrahedra units are also linked into different phosphorus oxygen groups by sharing oxygen atoms such as bisphosphonates, polyphosphate, and $(PO_3)_\infty$ chains. These P–O groups can bond with other ionic polyhedrons to build three-dimensional framework structures [2,4,9].

Among the phosphates, rubidium titanyl phosphate (RTP) crystal has significant technological applications in electro-optic shutters, Q-switches, and pulse selectors based on its large dielectric constant, high laser damage threshold, and stable physicochemical properties [10,11]. The three-dimensional crystal structure of RTP is made up of an alternating connection of [TiO_6] octahedral groups and [PO_4] tetrahedral groups, and the resulting cavities are occupied by the alkali metal Rb atoms [12,13]. Research indicates that the large-distortion of [TiO_6] octahedron in the structure plays a major role in the optical properties of titanium-containing phosphates [14]. As well as RTP, $RbTiP_2O_7$ and $RbTi_2(PO_4)_3$ materials, containing Rb, Ti, P, and O elements, were previously reported because of the potential technological interest [15,16].

As new kinds of phosphates, $Me_3Ti_3P_5O_{20}$ (Me stands for alkaline-earth metals) materials are non-centrosymmetric and contain [TiO_6] and [PO_4] functional units in the structure.

$K_3Ti_3P_5O_{20}$ crystal was first reported by Nagornyi et al. in 1993 and showed the potential application as a valuable NLO optical material [17]. $Rb_3Ti_3P_5O_{20}$ crystal is the second material reported for $Me_3Ti_3P_5O_{20}$ compounds, after $K_3Ti_3P_5O_{20}$ [18]. However, there are few studies on $Rb_3Ti_3P_5O_{20}$ crystals. The growth of bulk crystals and the property characterization were not carried out. In this work, $Rb_3Ti_3P_5O_{20}$ single crystals were grown by the high temperature solution growth (HTSG) method and measured via powder X-ray diffraction (XRD) and Infrared (IR) spectroscopy. The electronic structure was studied by X-ray photoelectron spectroscopy (XPS). Linear optical properties and nonlinear optical property (frequency-doubled effect) were investigated. With the aim to better explain the structure–property relation, the density functional theory (DFT) method was applied to compute the density of states (DOS), energy band structure, and linear refractive indices (n).

2. Materials and Methods

2.1. Single Crystal Growth

$Rb_3Ti_3P_5O_{20}$ single crystals were prepared by the HTSG method. The raw materials TiO_2 (99.9%, TianJin Chemical Reagent Factory, Tianjin, China), $NH_4H_2PO_4$ (99.5%, Sinopharm Chemical Reagent Co., Ltd., Shanghai, China), and Rb_2CO_3 (99.9%, Jiangxi Dongpeng New Materials Co., LTD., Jiangxi, China) were not subjected to any additional treatment. Rb_2CO_3, $NH_4H_2PO_4$, and TiO_2 were thoroughly mixed and adequately ground in a molar ratio of 9:20:3 and put into a Pt pot [18]. First, the Pt pot with the batch was heated to 700 °C in the furnace and held for 12 h until all the decomposed gases (NH_3, CO_2) were gone. Second, the mixture was put into a programmable temperature vertical resistance wire heating furnace and heated to 950 °C for 48 h. A platinum agitator blade was put into the solution for mechanical stirring for at least 36 h in order to increase the solution homogeneity. Third, the temperature of the solution was slowly decreased to 800 °C over two weeks and finally dropped to room temperature for seven days. Transparent colorless crystals were obtained from the excess flux by washing the cake in water.

2.2. Characterization

The XRD pattern was recorded by employing a Rigaku SmartLab 9KW X-ray diffractometer (Tokyo, Japan) set with the use of a Copper target X-ray source (λ = 0.15418 nm) in the diffraction angle range (2θ) of 10–60°. The measurement had a scanning step size of 0.02° and a scanning step time of 0.4 s at room temperature. A bulk transparent $Rb_3Ti_3P_5O_{20}$ single crystal ($0.12 \times 0.1 \times 0.1$ mm^3) was chosen for the analysis of single crystal structure. The single crystal diffraction data collection was recorded via a Bruker D8 VENTURE PHOTON 100 diffractometer (Karlsruhe, Germany) with the use of a monochromatic Molybdenum target X-ray source (λ = 0.71073 Å) at 296.15 K. The crystal structure was resolved with the SHELXT structure solution program via Intrinsic Phasing and polished up with the SHELXL refinement package by making use of least square minimization [19]. The precise crystallographic data and detailed experimental conditions of $Rb_3Ti_3P_5O_{20}$ crystal are listed in Table 1. Electron Probe Microanalysis (EPMA) was measured by a Shimadzu EPMA-1720H (Kyoto, Japan) for compositional analysis of the $Rb_3Ti_3P_5O_{20}$ crystal. A well-polished wafer was chose for measurement. XPS spectra were surveyed by an X-ray photoelectron spectrometer (Thermo Fisher ESCALAB 250, Waltham, MA, USA) in an ultra-high vacuum ($<10^{-7}$ Pa) with the use of a monochromatic aluminum target X-ray source. The excess charging on the sample surface during the measurement was neutralized by the neutralization gun [20].

Table 1. Crystal data and structure refinement for $Rb_3Ti_3P_5O_{20}$ crystal.

Formula	$Rb_3Ti_3P_5O_{20}$
Formula mass	874.96
Temperature (K)	296.15
Crystal system	orthorhombic
Space group	$Pca2_1$
a (Å)	18.2967(17)
b (Å)	6.3043(5)
c (Å)	14.7942(15)
α (°)	90
β (°)	90
γ (°)	90
Volume ($Å^3$)	1706.5(3)
Z	4
Density(cal.) (g/cm^3)	3.406
μ (mm^{-1})	10.450
F (000)	1648.0
Crystal size (mm^3)	0.12 × 0.1 × 0.1
Radiation	Mo Kα (λ = 0.71073)
2θ range for data collection (°)	4.452 to 72.844
Index ranges	$-14 \leq h \leq 30$, $-10 \leq k \leq 8$, $-24 \leq l \leq 24$
Reflections collected	23,890
Independent reflections	8114 [R_{int} = 0.0457, R_{sigma} = 0.0540]
Data/restraints/parameters	8114/1/282
Goodness-of-fit on F^2	1.010
Final R indexes [$I \geq 2\sigma$ (I)]	R_1 = 0.0345, wR_2 = 0.0826
Final R indexes [all data]	R_1 = 0.0429, wR_2 = 0.0864
Largest diff. peak/hole (e $Å^{-3}$)	2.02/−1.81
Flack parameter	0.029(9)

IR spectra were measured with a Nicolet NEXUS 670 infrared spectrometer (Thermo Nicolet Corporation, Madison, WI, USA). Fully ground crystalline powders were used for testing. Ultraviolet-Visible (UV-Vis) diffuse reflectance data for $Rb_3Ti_3P_5O_{20}$ crystals were obtained by using a Hitachi UH4150 spectrophotometer (200–800 nm, Tokyo, Japan). The optical transmission spectra were measured on a Hitachi UH4150 UV-Vis-IR spectrometer (200–2000 nm) and a Nicolet NEXUS 670 FTIR spectrometer (2000–5000 nm) using a well-polished crystal wafer of $Rb_3Ti_3P_5O_{20}$. The frequency-doubling effect of $Rb_3Ti_3P_5O_{20}$ crystal was tested on a Q-switched Nd:YAG solid-state laser under a 1064 nm wavelength by the Kurtz–Perry technique, and a KDP was used as a reference [21]. The test conditions were not changed after the test start to ensure the accuracy of the results.

2.3. Computational Details

The electronic structure of $Rb_3Ti_3P_5O_{20}$ was calculated by the ultra-soft pseudopotential method using DFT in the CASTEP module including density of states (DOS), band structure (Eg) and refractive indices (n) [22]. The 3D crystallographic structure file from single crystal structure determination of $Rb_3Ti_3P_5O_{20}$ crystals was used for optimization and calculation. During the numerical calculation, generalized gradient approximation and Perdew–Burke–Ernzerhof functions were used to optimize the total energy of the system to a minimum. Thereby, the Rb $4p^65s^1$, Ti $3p^64s^23d^2$, P $3s^23p^{3,}$ and O $2s^22p^4$ states were considered as the valence electrons. The K point mesh was set as 2 × 6 × 3 in the Brillouin region and the cut-off limit of kinetic energy was set at 350 eV. The refractive indices and birefringence of the $Rb_3Ti_3P_5O_{20}$ crystal were computed based on the obtained band structure and DOS.

3. Results and Discussion

3.1. Crystal Growth

Due to the high thermal stability of the $Rb_3Ti_3P_5O_{20}$ crystal, it can be grown below the melting point using the high temperature solution method [18]. To obtain high quality crystals, it is extremely vital to choose an appropriate flux. Previously, for decreasing the viscosity of the melt and the melting point, Rb_2CO_3 and $NH_4H_2PO_4$ fluxes were utilized in our laboratory to grow high quality single crystals of pure RTP and doped-RTP [13,23,24]. Therefore, we have chosen Rb_2CO_3 and $NH_4H_2PO_4$ to serve as fluxes for growing $Rb_3Ti_3P_5O_{20}$ single crystals. As a result, the millimeter-sized transparent colorless single crystals were successfully obtained. Figure 1a shows the photograph of as-grown $Rb_3Ti_3P_5O_{20}$ crystals with dimensions of $7 \times 2 \times 1$ mm^3 and $3 \times 3 \times 1$ mm^3. The experimental powder XRD of $Rb_3Ti_3P_5O_{20}$ crystal is plotted in Figure 1b. The diffraction peak positions of as-grown crystals correspond well to a standard $Rb_3Ti_3P_5O_{20}$ pattern (PDF No. 82-1169) [18], suggesting that the $Rb_3Ti_3P_5O_{20}$ crystals possess not only high purity but also good crystallinity. Meanwhile, the Rietveld refinement of XRD was carried out by GSAS 2 software and the final plot is shown in Figure 2. The compositional analysis of $Rb_3Ti_3P_5O_{20}$ crystal shows that elemental ratios of Rb, Ti, P, and O are 3.55:3.25:6.12:20.42.

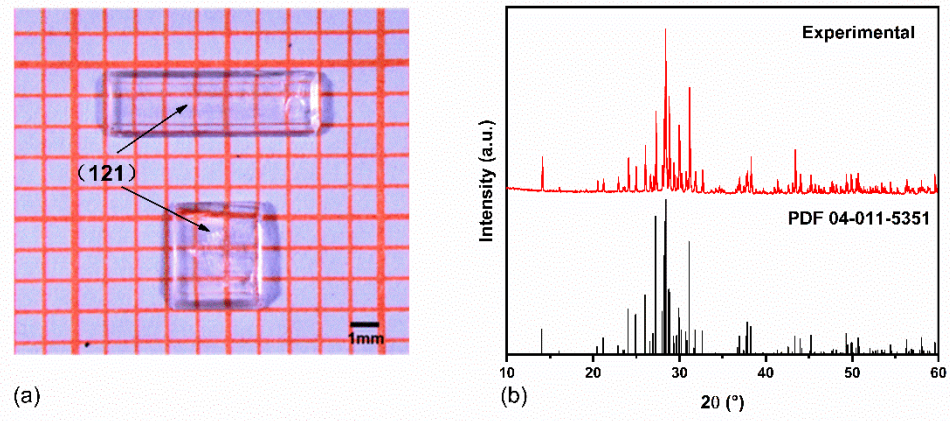

Figure 1. (**a**) The photograph of the $Rb_3Ti_3P_5O_{20}$ single crystals. The crystal faces are all perpendicular to the page (121); (**b**) X-ray powder diffraction pattern of the as-grown $Rb_3Ti_3P_5O_{20}$ single crystal.

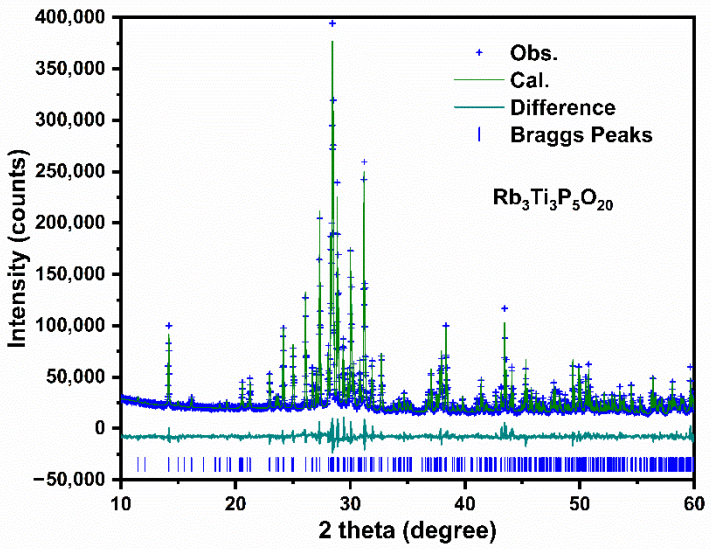

Figure 2. The Rietveld refinement results of $Rb_3Ti_3P_5O_{20}$. Obs. = observed date, Cal. = calculated date, Difference = Obs.−Cal., Braggs Peaks represent the diffractions peak positions.

3.2. Crystal Structure

The structure of the $Rb_3Ti_3P_5O_{20}$ crystal was obtained by single crystal XRD analysis. It belongs to an orthogonal crystal system with a polar space group of $Pca2_1$ (No. 29) with the unit cell parameters a = 18.2967(17) Å, b = 6.3043(5) Å, c = 14.7942(15) Å, and Z = 4. The unit cell parameters are similar to those reported in a paper (a = 18.282(2) Å, b = 6.2932(7) Å, c = 14.773(2) Å) [18]. The structure diagram of the $Rb_3Ti_3P_5O_{20}$ crystal along the b-axis is plotted in Figure 3a. It features a three-dimensional (3D) structure consisting of [TiO_6] and [PO_4] polyhedrons, linked via P–O–P, P–O–Ti and Ti–O–Ti bonds. The Rb atoms are ten-coordinated or eleven-coordinated by oxygen atoms to maintain electrical neutrality, and they are located in the one-dimensional channels. The Ti–O and P–O bond lengths are in the regions 1.797–2.031 Å and 1.483–1.615 Å, respectively. The O–P–O and the O–Ti–O angles in the $Rb_3Ti_3P_5O_{20}$ crystal are in the ranges 98.9°–116.8° and 84.89°–177.95°.

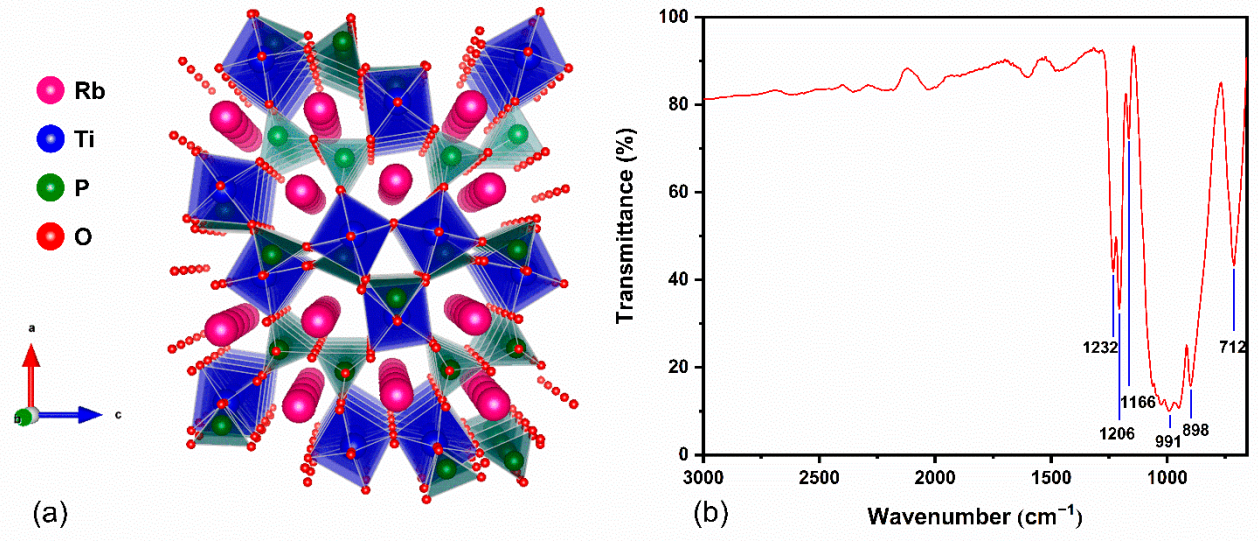

Figure 3. (**a**) The crystal structure of $Rb_3Ti_3P_5O_{20}$ crystal (Rb–O bonds are deleted for clarity); (**b**) IR spectra of $Rb_3Ti_3P_5O_{20}$.

For the purpose of further verifying the types of phosphorus oxygen groups in $Rb_3Ti_3P_5O_{20}$ structure, IR spectra (Figure 3b) were measured for the 600–3000 cm^{-1} wavenumbers. The peaks of 1232, 1206, and 1166 cm^{-1} are attributable to the asymmetric stretching vibrations of P–O bonds. The IR spectra, ranging from 800 to 1100 cm$^{-1,}$ are assigned to the symmetric stretching vibrations and the asymmetric stretching vibrations of P–O–P. The peak of 712 cm^{-1} is caused by the symmetric stretching vibrations of P–O–P. Hence, the IR spectra specify the existence of [PO_4] tetrahedron and [P_2O_7] dimer, which coincide with the results obtained from the single crystal structure analysis of related phosphates [25,26].

3.3. Electronic Structure

The electronic structure of the $Rb_3Ti_3P_5O_{20}$ crystal was first measured by XPS and analyzed. The survey spectrum recorded for the $Rb_3Ti_3P_5O_{20}$ single crystal is shown in Figure 4a. The characteristic peaks of all constituent elements (Rubidium, Titanium, Phosphorus, and Oxygen) were found in the survey spectrum. The C 1s peak (284.6 eV) was attributed to hydrocarbonate contamination, and the line was used as a reference for the binding energy scale calibration. The calcium element was also tested as surface contamination.

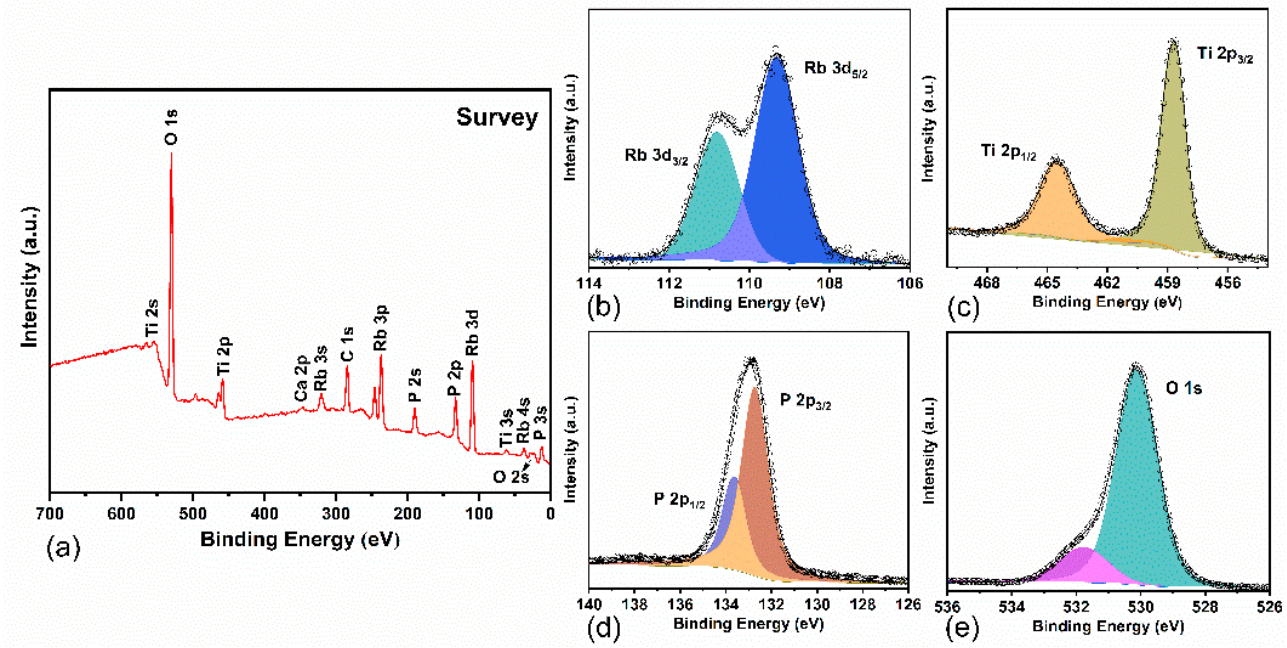

Figure 4. (**a**) Survey XPS spectrum of $Rb_3Ti_3P_5O_{20}$ crystal. The corresponding element peaks are marked in the spectrum; (**b**–**e**) High resolution XPS spectra recorded for $Rb_3Ti_3P_5O_{20}$ crystal.

The deconvoluted high-resolution XPS spectra [27,28], of major elements in $Rb_3Ti_3P_5O_{20}$ crystal are shown in Figure 4b–e. The binding energy (BE) values and the BE difference of the constituent elements of the title compound are presented in Table 2. $RbTiOPO_4$ (RTP) and $KTiOPO_4$ (KTP) are given for comparison. The BE values of Rb $3d_{5/2}$, Ti $2p_{3/2}$, P 2p, and O 1s for $Rb_3Ti_3P_5O_{20}$ crystal are 109.3 eV, 458.6 eV,132.7 eV, and 530.1 eV, respectively. The main peak of O 1s at 530.1 eV corresponds to lattice oxygen. The weak peak at 531.8 eV is usually attributed to defects and contamination (such as H_2O and CO_2) of the material surface. The BE values are similar to those of the corresponding elements in RTP and KTP crystals, and this indicates that the atoms are in similar chemical environments [29,30]. The BE difference ΔBE (M–O) = BE (O 1s)—BE(M), where M is the element to be analyzed, is usually used to evaluate the chemical bonding of the elements in crystal lattice because the parameters are insensitive to the surface charging effects [31–33]. As for $Rb_3Ti_3P_5O_{20}$, the BE difference values were calculated to be as follows: ΔBE (Ti–O) = 71.5 eV, ΔBE (P–O) = 397.4 eV and ΔBE (Rb–O) = 420.8 eV, respectively. Compared with RTP, $Rb_3Ti_3P_5O_{20}$ shows smaller ΔBE (O–Ti) and ΔBE (O–P) values. The results demonstrate that the $Rb_3Ti_3P_5O_{20}$ crystal exhibits weaker covalency of P–O bonds and stronger ionicity of Ti–O bonds compared with RTP.

Table 2. Binding energy values (eV) of $Rb_3Ti_3P_5O_{20}$, RTP, and KTP crystals.

	$Rb_3Ti_3P_5O_{20}$	RTP	KTP
Rb $3d_{5/2}$ (±0.1 eV)	109.3	108.9	–
Ti $2p_{3/2}$ (±0.1 eV)	458.6	458.6	458.4
P 2p (±0.1 eV)	132.7	132.8	132.8
O 1s (±0.1 eV)	530.1	530.4	530.9
ΔBE (O 1s−Rb 3d)	420.8	421.5	–
ΔBE (O 1s−Ti 2p)	71.5	71.8	72.5
ΔBE (O 1s−P 2p)	397.4	397.6	398.1
Reference	This work	[29]	[30]

3.4. Optical Properties Characterization

The UV-Vis diffuse reflectance spectrum of $Rb_3Ti_3P_5O_{20}$ crystals is shown in Figure 5a. The absorption data were calculated based on reflection spectra by using the Kubelka–Munk transformation equation:

$$F(R) = K/S = (1 - R)^2/(2R) \quad (1)$$

where S is the scattering coefficient, K is the absorption coefficient, and R is the reflectance [34]. The optical band gap of $Rb_3Ti_3P_5O_{20}$ crystals is estimated to be 3.54 eV, which is corresponding to the absorption edge of 339 nm. For further obtaining a precise value of the absorption edge, the transmission spectrum (200–5000 nm) of a well-polished wafer was recorded. Figure 5b demonstrates that the transmission cutoff edge can reach down to 331 nm in the UV region, which is shorter compared with the RTP crystal (350 nm). The IR region cutoff edge of $Rb_3Ti_3P_5O_{20}$ crystal is located at 4.5 μm. This shows the similarity to the KTP and RTP crystals. The $Rb_3Ti_3P_5O_{20}$ crystal is of high transparency in the UV-Vis-NIR region and has a wide optical transparency range of 0.33–4.5 μm. The step near 800 nm is caused by a test instrument (light source change). The absorption band at 3000 nm may be related to the formation of hydrogen bonds in the crystal (stretching vibrations of the O-H bond).

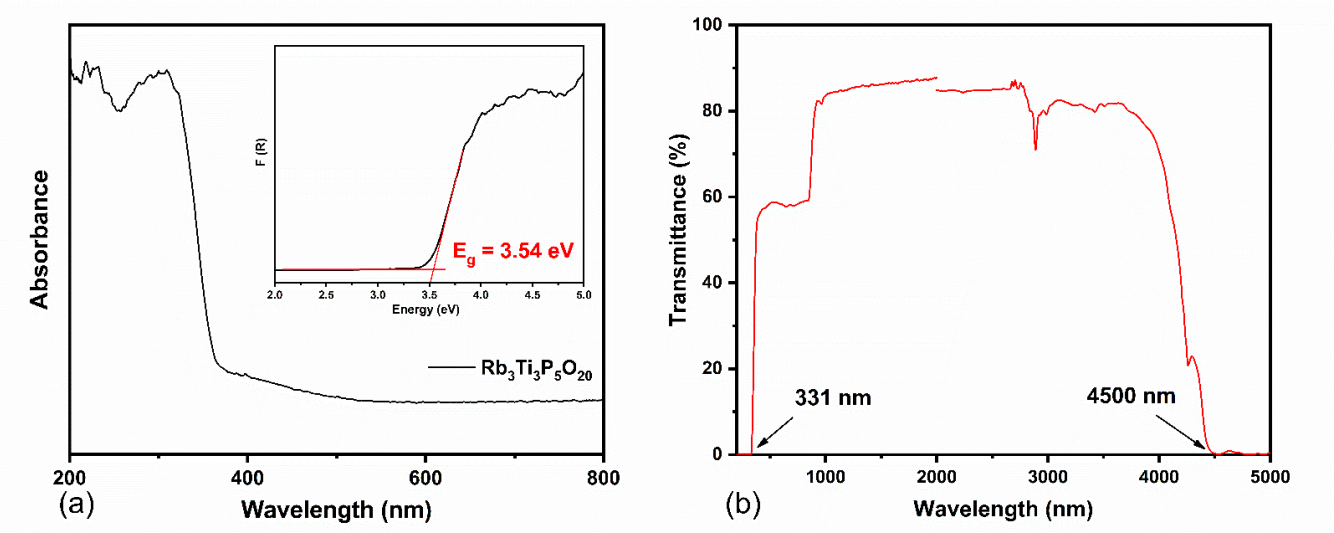

Figure 5. (**a**) UV-Vis diffuse reflectance spectra of $Rb_3Ti_3P_5O_{20}$ crystal. The inset displays the experimental band gap; (**b**) UV-vis and IR transmission spectra of the $Rb_3Ti_3P_5O_{20}$ crystal.

The SHG response was measured because $Rb_3Ti_3P_5O_{20}$ crystal is non-centrosymmetric. The result is plotted in Figure 6. The SHG intensity is about 0.4 × KDP for a particle size range of 70–90 μm. The magnitudes of distortions of the TiO_6 octahedra were calculated using the method proposed by P. Shiv Halasyamani [35]. The magnitude of the distortion was quantified by considering deviations from 180° of the three trans O–Ti–O bond angles as well as the six Ti–O bond distances in the [TiO_6] octahedra. The calculation formula of the octahedral distortion (Δd) is as follows:

$$\Delta d = \frac{|(M-O1)-(M-O4)|}{|\cos\theta_1|} + \frac{|(M-O2)-(M-O5)|}{|\cos\theta_2|} + \frac{|(M-O3)-(M-O6)|}{|\cos\theta_3|} \quad (2)$$

where the oxygen pairs (O1, O4) are in opposite positions in the [TiO_6] octahedra. (O2, O5) and (O3, O6) are positioned in the same way. The calculated Δd values for [TiO_6] octahedra with three different crystallographic positions are 0.1536, 0.2631, and 0.2909, respectively. According to the definition of P. Shiv Halasyamani, these values belong to a weak distortion range (0.05–0.40) [35]. The weak distortions of [TiO_6] octahedra might result in a weak SHG response of the $Rb_3Ti_3P_5O_{20}$ crystal.

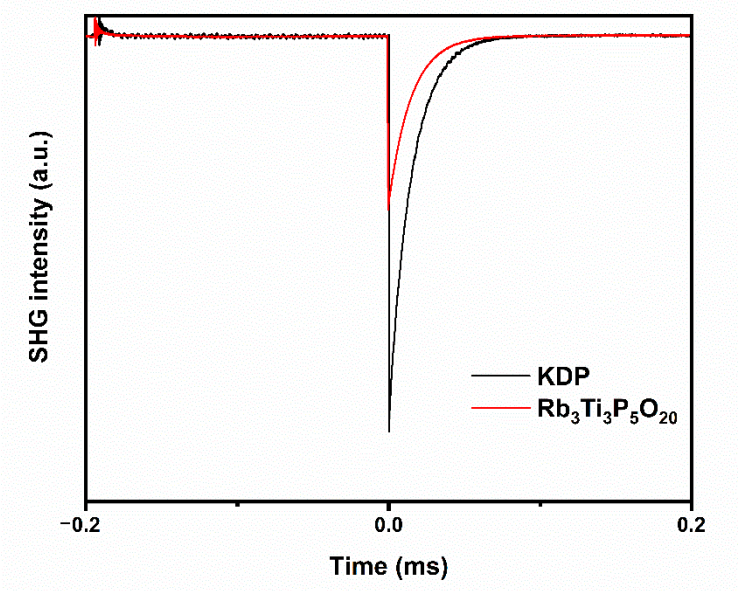

Figure 6. The SHG signals for $Rb_3Ti_3P_5O_{20}$ and KDP standard sample.

3.5. Theoretical Calculations

To explore the structure–property relationship of the $Rb_3Ti_3P_5O_{20}$ crystals, the band structure and DOS were calculated based on the DFT method. As shown in Figure 7a, $Rb_3Ti_3P_5O_{20}$ is an indirect band gap material with an energy band gap width of 2.79 eV, which is smaller than the test value (3.54 eV). It can be attributed to the underestimation of the band gap by the DFT method [36]. The calculated total densities of states and partial densities of states (TDOS and PDOS) are plotted in Figure 7b. Optical properties of crystals are closely related to electronic transitions near the Fermi level (or the forbidden band). Therefore, it is vital to investigate the valence band top (VBT) and the conduction band bottom (CBB).

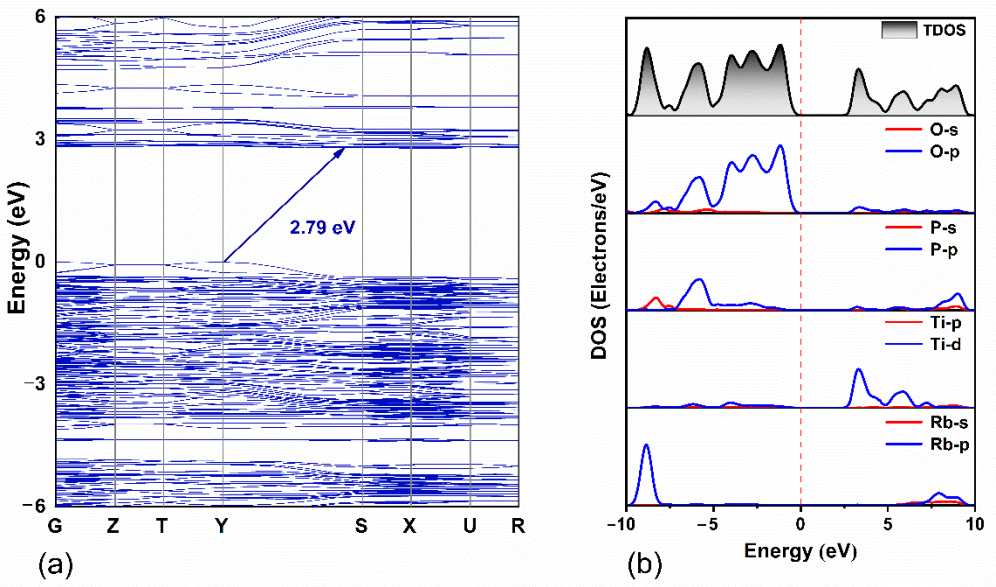

Figure 7. Theoretical calculation of $Rb_3Ti_3P_5O_{20}$. (**a**) Energy band structure; (**b**) TDOS and PDOS curves. The dashed line in the figure is the Fermi energy level (0.0 eV).

From the spectra shown in Figure 7b, it can be inferred that: (1) the orbital effect of alkali metal cations (Rb^+) to electronic transitions near the forbidden band can be negligible. (2) the electronic states of VBT between –5.0 eV and 0.0 eV are mainly constituted by O 2p

orbitals and a spot of P 3p orbitals. (3) the electronic states near CBB (2.7 eV–5.0 eV) are mainly contributed by Ti 3d orbitals and little component O 2p orbitals. According to these analyses, it is clear that distorted [TiO_6] octahedra contribute considerably to the optical properties of $Rb_3Ti_3P_5O_{20}$ crystals, while [PO_4] and [P_2O_7] groups contribute less to the optical properties. Based on the calculated energy band structure and DOS, linear refractive index curves and birefringence (Δn) curve of $Rb_3Ti_3P_5O_{20}$ are computed. As shown in Figure 8, the refractive indices are characterized by a considerable anisotropy and $n_x > n_z > n_y$, which indicates that the $Rb_3Ti_3P_5O_{20}$ is a biaxial crystal. The values of the birefringence are 0.079 at 1064 nm and 0.104 at 532 nm. The relatively large birefringence at 1064 nm of $Rb_3Ti_3P_5O_{20}$ is close to the value of KTP (experimental Δn = 0.092 at 1064 nm).

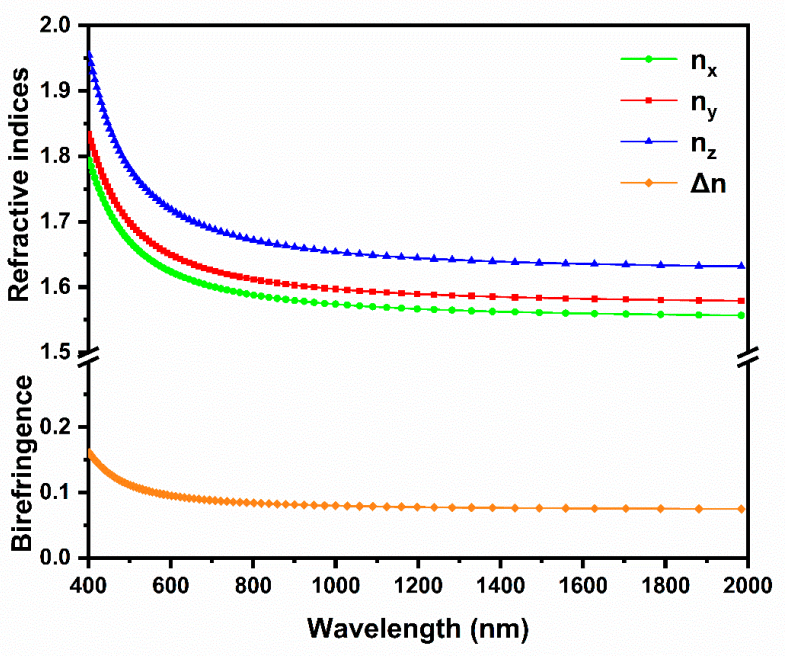

Figure 8. Calculated dispersive refractive index and Birefringence curves.

4. Conclusions

In summary, large $Rb_3Ti_3P_5O_{20}$ single crystals with dimensions of 7 × 2 × 1 mm^3 and 3 × 3 × 1 mm^3 were successfully grown via the high temperature solution growth method in the Rb_2O–TiO_2–P_2O_5 system. The structural analysis indicates that there are two anionic groups [PO_4] and [P_2O_7] in the structure of $Rb_3Ti_3P_5O_{20}$ crystal. The optical properties of the crystal, including UV-Vis diffuse reflectance spectra and transmission spectra, were studied for the first time. The results demonstrated that $Rb_3Ti_3P_5O_{20}$ displays a wide transparent range of 0.33–4.5 μm and has a relatively large band gap of 3.54 eV. The second harmonic generation measurement showed that the SHG intensity is about 0.4 × KDP. The weak distortions of [TiO_6] octahedra might result in the weak SHG response. The band structure, the density of states, and the dispersive refractive indices were calculated by first principles calculations. The DOS spectra of $Rb_3Ti_3P_5O_{20}$ show that the valence band top is formed mainly by O 2p orbitals and the conduction band bottom is contributed to by Ti 3d orbitals. Therefore, distorted [TiO_6] octahedra contributes considerably to the optical properties. Furthermore, $Rb_3Ti_3P_5O_{20}$ has a moderate birefringence of 0.079 at 1064 nm. This work may be used as a reference for feasible optical application prospects of $Rb_3Ti_3P_5O_{20}$ crystals.

Author Contributions: J.Z. and X.D. conceived and designed the research and wrote the manuscript. J.Z. carried out all of the experiments. P.Z. and F.Y. were involved in the theoretical calculation and optical performance analysis. Z.W. and L.A. were involved in the electronic structure measurement and analysis. All authors have read and agreed to the published version of the manuscript.

Funding: This work was supported by grant from the National Natural Science Foundation of China (No. 51672160).

Institutional Review Board Statement: Not applicable.

Informed Consent Statement: Not applicable.

Data Availability Statement: The data presented in this study are available on request from the corresponding author.

Conflicts of Interest: The authors declare no conflict of interest.

References

1. Zatovsky, I.V.; Strutynska, N.Y.; Slobodyanik, N.S.; Baumer, V.N.; Shishkin, O.V. Synthesis and characterization of phosphates in the pseudo-ternary melted systems Cs_2O-P_2O_5-$M^{II}O$ (M^{II}—Alkaline earth). *Cryst. Res. Technol.* **2008**, *43*, 362–368. [CrossRef]
2. Huang, S.; Jing, Q.; Han, J.; Pan, S.; Wu, H.; Yang, Z. Three Alkali Metal Lead Orthophosphates—Syntheses, Crystal Structures and Properties of $APbPO_4$ (A = K, Rb, Cs). *Eur. J. Inorg. Chem.* **2015**, *2015*, 1490–1495. [CrossRef]
3. Essehli, R.; El Bali, B.; Benmokhtar, S.; Fuess, H.; Svoboda, I.; Obbade, S. Synthesis, crystal structure and infrared spectroscopy of a new non-centrosymmetric mixed-anion phosphate $Na_4Mg_3(PO_4)_2(P_2O_7)$. *J. Alloy. Compd.* **2010**, *493*, 654–660. [CrossRef]
4. Dong, X.; Shi, Y.; Zhang, M.; Chen, Z.; Jing, Q.; Yang, Y.; Pan, S.; Yang, Z.; Li, H. The Flexibility of P_2O_7 Dimers in Soft Structures: $M_2CdP_2O_7$ (M = Rb, Cs). *Eur. J. Inorg. Chem.* **2016**, *2016*, 2704–2708. [CrossRef]
5. Li, Y.; Liang, F.; Song, H.; Liu, W.; Lin, Z.; Zhang, G.; Wu, Y. $CsLiMgP_2O_7$: A congruently melting pyrophosphate with a $[LiMgP_4O_{18}]^{6-}$ membered ring fundamental building block. *Solid State Sci.* **2019**, *91*, 23–27. [CrossRef]
6. Phan, V.T.; Do, T.T.P.; Ho, T.M.; Nguyen, D.T.; Le, B.V.; Le, A.T.Q.; Duong, P.A.; Huynh, D.T. Fabrication of KDP crystal prisms for second harmonic generation. *Optik* **2018**, *171*, 230–236. [CrossRef]
7. Roth, M.; Angert, N.; Tseitlin, M.; Alexandrovski, A. On the optical quality of KTP crystals for nonlinear optical and electro-optic applications. *Opt. Mater.* **2001**, *16*, 131–136. [CrossRef]
8. Wang, Y.; Zhang, J.; Xue, J.; Zhang, K.; Wen, L.; Liang, G. Effect of particle dispersion on the properties of $LiFePO_4$ slurry and the electrochemical properties of the battery. *Ionics* **2022**, *28*, 1547–1558. [CrossRef]
9. Chen, W.; Jing, Q.; Zhang, Q.; Lee, M.-H.; Lu, X.; Wei, P.; Chen, Z. A New Cadmium-Based $Pb_2Cd_3(PO_4)_2(P_2O_7)$ with Two Types of Isolated P-O Groups. *Eur. J. Inorg. Chem.* **2019**, *2019*, 1273–1278. [CrossRef]
10. Kannan, C.V.; Moorthy, S.G.; Kannan, V.; Subramanian, C.; Ramasamy, P. TSSG of $RbTiOPO_4$ single crystals from phosphate flux and their characterization. *J. Cryst. Growth* **2002**, *245*, 289–296. [CrossRef]
11. Shang, L.H.; Wen, Y.; Li, T.Y.; Guo, Y.Y.; Wang, Y.H.; Wu, C.T.; Wang, C.; Jin, G.Y. Pulse peaks synchronize dual-wavelength laser based on Q-switch delay trigger. *Infrared Phys. Technol.* **2021**, *116*, 103751. [CrossRef]
12. Liu, J.; Li, Z.; Zhu, P.; Duan, X. Crystal growth, electronic structure and luminescence properties of Nb/Yb co-doped $RbTiOPO_4$ crystals. *Opt. Mater.* **2018**, *75*, 38–43. [CrossRef]
13. Li, Z.; Chen, Y.; Zhu, P.; Ji, N.; Duan, X.; Jiang, H. Top-seeded solution growth and morphology change of $RbTiOPO_4$:Ta single crystal. *J. Cryst. Growth* **2018**, *487*, 87–91. [CrossRef]
14. Novikova, N.; Sorokina, N.; Verin, I.; Alekseeva, O.; Orlova, E.; Voronkova, V.; Tseitlin, M. Structural Reasons for the Nonlinear Optical Properties of KTP Family Single Crystals. *Crystals* **2018**, *8*, 283. [CrossRef]
15. Shumin, W.; Hwu, S.-J. Completion of the Alkali Metal Titanium (III) and Pyrophosphate Series: Synthesis and Structure of $ATiP_2O_7$ (A = K, Rb, Cs). *J. Solid State Chem.* **1991**, *92*, 219–226.
16. Hazen, R.M.; Palmer, D.C.; Finger, L.W.; Stuckyg, G.D.; Harrison, W.T.A.; Gier, T.E. High-pressure crystal chemistry and phase transition of $RbTi_2(PO_4)_3$. *J. Phys. Condens. Matter* **1994**, *6*, 1333–1344. [CrossRef]
17. Nagornyi, P.G.; Kapshuk, A.A. Synthesis and Structure of the Double Phosphate $K_3Ti_3P_5O_{20}$. *ChemInform Abstr.* **1993**, *24*, 11–13.
18. Duhlev, R. $Rb_3Ti_2(TiO)(PO_4)_3P_2O_7$: A New NonCentrosymmetric Titanyl Phosphate. *Acta Crystallogr. Sect. C* **1994**, *50*, 1523–1525. [CrossRef]
19. Sheldrick, G.M. Crystal structure refinement with SHELXL. *Acta Cryst. C Struct. Chem.* **2015**, *71*, 3–8. [CrossRef]
20. Duan, X.; Liu, J.; Chen, Y.; Li, Z.; Zhu, P.; Jiang, H. Modification of $RbTiOPO_4$ (001) crystal surface induced by Ar^+ ion bombardment: X-ray photoelectron spectroscopy and first-principles studies. *Vacuum* **2018**, *147*, 38–44. [CrossRef]
21. Zhao, S.; Gong, P.; Bai, L.; Xu, X.; Zhang, S.; Sun, Z.; Lin, Z.; Hong, M.; Chen, C.; Luo, J. Beryllium-free $Li_4Sr(BO_3)_2$ for deep-ultraviolet nonlinear optical applications. *Nat. Commun.* **2014**, *5*, 4019. [CrossRef]
22. Baiheti, T.; Han, S.; Tudi, A.; Yang, Z.; Pan, S. Alignment of Polar Moieties Leading to Strong Second Harmonic Response in $KCsMoP_2O_9$. *Chem. Mater.* **2020**, *32*, 3297–3303. [CrossRef]

23. Li, Z.; Zhu, P.; Ding, J.; Ji, N.; Chen, Y.; Wang, Z.; Duan, X.; Jiang, H. Increased Concentration of Yb^{3+} and High Crystal Field Strength in $RbTiOPO_4$:Ta Single Crystal with Optimized Growth. *Cryst. Growth Des.* **2019**, *19*, 7143–7152. [CrossRef]
24. Zhu, P.; Li, Z.; Chen, Y.; Duan, X. Growth, phase and electronic structure of $RbTiOPO_4$ crystals doped with antimony. *J. Cryst. Growth* **2018**, *486*, 91–95. [CrossRef]
25. Qi, L.; Chen, Z.; Li, L.; Jing, Q.; Li, N.; Jiang, Z.; Dong, X.; Lee, M.H. $A_2BBi_2(PO_4)_2(P_2O_7)$(A = K, Rb, B = Pb, Cd): The Effect of Cation Sizes on Structural Evolution. *Eur. J. Inorg. Chem.* **2020**, *2020*, 4007–4014. [CrossRef]
26. Wen, M.; Wu, H.; Wu, X. Influence of Cation on the Anion Frameworks and Properties of Four Lead Phosphates, $A_2PbBi_2(PO_4)_2(P_2O_7)$ (A = Rb, Cs) and $A_2PbP_2O_7$ (A = K, Rb). *Inorg Chem* **2020**, *59*, 2945–2951. [CrossRef]
27. Torres-Cavanillas, R.; Morant-Giner, M.; Escorcia-Ariza, G.; Dugay, J.; Canet-Ferrer, J.; Tatay, S.; Cardona-Serra, S.; Gimenez-Marques, M.; Galbiati, M.; Forment-Aliaga, A.; et al. Spin-crossover nanoparticles anchored on MoS_2 layers for heterostructures with tunable strain driven by thermal or light-induced spin switching. *Nat. Chem.* **2021**, *13*, 1101–1109. [CrossRef]
28. Sanchis-Gual, R.; Torres-Cavanillas, R.; Coronado-Puchau, M.; Gimenez-Marques, M.; Coronado, E. Plasmon-assisted spin transition in gold nanostar@spin crossover heterostructures. *J. Mater. Chem. C Mater.* **2021**, *9*, 10811–10818. [CrossRef]
29. Atuchin, V.V.; Kesler, V.G.; Meng, G.; Lin, Z.S. The electronic structure of $RbTiOPO_4$ and the effects of the A-site cation substitution in $KTiOPO_4$-family crystals. *J. Phys. Condens. Matter* **2012**, *24*, 405503. [CrossRef]
30. Atuchin, V.V.; Kesler, V.G.; Maklakova, N.Y.; Pokrovsky, L.D.; Semenenko, V.N. Study of KTiOPO4 surface by x-ray photoelectron spectroscopy and reflection high-energy electron diffraction. *Surf. Interface Anal.* **2002**, *34*, 320–323. [CrossRef]
31. Atuchin, V.V.; Aleksandrovsky, A.S.; Chimitova, O.D.; Diao, C.P.; Gavrilova, T.A.; Kesler, V.G.; Molokeev, M.S.; Krylov, A.S.; Bazarov, B.G.; Bazarova, J.G.; et al. Electronic structure of beta-$RbSm(MoO_4)_2$ and chemical bonding in molybdates. *Dalton Trans.* **2015**, *44*, 1805–1815. [CrossRef] [PubMed]
32. Atuchin, V.V.; Kesler, V.G.; Pervukhina, N.V.; Zhang, Z. Ti 2p and O 1s core levels and chemical bonding in titanium-bearing oxides. *J. Electron Spectrosc. Relat. Phenom.* **2006**, *152*, 18–24. [CrossRef]
33. Atuchin, V.V.; Vinnik, D.A.; Gavrilova, T.A.; Gudkova, S.A.; Isaenko, L.I.; Jiang, X.; Pokrovsky, L.D.; Prosvirin, I.P.; Mashkovtseva, L.S.; Lin, Z. Flux Crystal Growth and the Electronic Structure of $BaFe_{12}O_{19}$ Hexaferrite. *J. Phys. Chem. C* **2016**, *120*, 5114–5123. [CrossRef]
34. Ding, J.; Zhu, P.; Li, Z.; Wang, Z.; Ai, L.; Zhao, J.; Yu, F.; Duan, X.; Jiang, H. Synthesis, electronic structure and upconversion photoluminescence of langbeinite-type $K_2TiYb(PO_4)_3$ microcrystals. *Optik* **2021**, *244*, 167549. [CrossRef]
35. Halasyamani, P.S. Asymmetric Cation Coordination in Oxide Materials: Influence of Lone-Pair Cations on the Intra-octahedral Distortion in d^0 Transition Metals. *Chem. Mater.* **2004**, *16*, 3586–3592. [CrossRef]
36. Lu, W.; Gao, Z.; Liu, X.; Tian, X.; Wu, Q.; Li, C.; Sun, Y.; Liu, Y.; Tao, X. Rational Design of a $LiNbO_3$-like Nonlinear Optical Crystal, Li_2ZrTeO_6, with High Laser-Damage Threshold and Wide Mid-IR Transparency Window. *J. Am. Chem. Soc.* **2018**, *140*, 13089–13096. [CrossRef]